Calculation of the influence of solid-phase concentration on sewage pumps based on Mixture model

LI Xin, ZHANG Yu-liang, YU Jian-ping, ZHOU Zhao-zhong

***Abstract*— The steady flow of the internal flow field in a sewage pump was numerically simulated and analyzed as a solid–liquid two-phase flow was transported. The simulation and analysis were based on the mixture multiphase model, the RNG k–ε turbulence model, the frozen rotor method, and the SIMPLE algorithm. The impact of the solid–liquid two-phase flow on the hydraulic performance of the sewage pump and the attrition rate of the vane was emphatically analyzed under different solid-phase concentrations. Results show that, as the concentration of the transported solid phase increased, the pump lift and efficiency decreased monotonously. The shaft power also showed a tendency to monotonically increase. The solid-phase concentration on the pressure surface of the vane continuously increased as well. Under a high transportation concentration, the secondary part of the suction surface experienced the most severe wear. The equilibrium point of equal pressure continuously moved toward the leading edge of the vane. At the same time, the isoconcentration points of the pressure surface and suction surface moved toward the vane inlet.**

***Index Terms*— sewage pump; solid-phase concentration; numerical calculation; hydraulic performance; attrition rate**

I. INTRODUCTION

Sewage pumps are solid–liquid pumps that are commonly used to clear channel sedimentation in cities. Researchers at home and abroad have conducted in-depth studies on sewage pumps and have made important achievements. Engin carried out experiments to compare transported mediums with various levels of hardness, such as water and sand. On the basis of the different capabilities of the centrifugal pump with a semi-enclosed impeller pump in the experiment, Engin derived a conclusion on the relation between particle size and pump capability. During the liquid–solid transport process, the predictive data on the lift and deviation of the experiment value ranged from −20% to 15％ [1]. Gandhi performed an experiment to test the capacity of a centrifugal pump with a shrouded impeller when the transmission medium was a mixture of water, mortar, and tailing containing zinc mineral. When the solid concentration was lower than 20%, the relation between the pump lift and the flow could be determined by calculating the pure water condition. Yuan Qi et al. [3] investigated a non-overload mud pump through a numerical simulation and found the existence of backflow at the entry and velocity slip between two phases. At the junction of the pressure surface and suction surface, the turbulent kinetic energy and turbulent kinetic energy dissipation rate of the liquid phase reached their extreme points. Li et al. [4] investigated the influence of solid particles of different diameters on the external characteristics of a centrifugal pump. Under a small flow condition, the efficiency value slightly increased; the stable working range shrank, and the best efficiency point moved toward the small flow.

Zhang et al. conducted a numerical simulation for a two-phase flow field in a centrifugal pump by using the numerical calculation method. Distinct jet-wake flows were observed near the volute tongue. As the volume fraction increased, the jet-wake flows became increasingly obvious. Another numerical simulation was also performed to investigate the starting characteristics of a centrifugal pump with a high specific speed for transporting solid–liquid two-phase flows [6]. Harry et al. [7] investigated centrifugal pump vanes made from high chromium cast iron and aluminum alloy by using the Coriolis experiment. The centrifugal pump vanes showed different wear patterns when the transmission medium was slurry. On the basis of a rapid experiment and mathematical analysis, Veselin et al. [8] proposed a type of wear forecast method that could replace traditional mud pump wear tests, which are time consuming and costly and involve poor validation.

Most designs of sewage pumps are based on former designs. Thus, an effective pump performance is difficult to guarantee. In this context, an extensive investigation into the internal flow of pumps is urgently necessary. The findings of such investigation can then be used to derive a theoretical basis for developing a type of pump with high standard performance and stable operation. The present work presents numerical simulations and analyses of a solid–liquid two-phase pump and emphasizes the impact of the solid–liquid two-phase flow on the performance of the sewage pump in terms of solid-phase concentration. Through the analysis of the internal pressure and dynamic deposition distribution of the particles on the surface of the solids, we can perform a preliminary forecast of the basic characteristics of a sewage pump and thereby derive a theoretical basis for improving the design of sewage pumps.

II. PUMP MODEL AND CALCULATION METHOD

2.1 Pump model and computational grid

The calculation model was a centrifugal pump with a specific speed of ns=129.3. The fundamental performance parameters are as follows: flux, 50 m^3/h; lift, 20.54 m; rotation rate, 2900 r/min. The main geometry sizes of the pump are as follows: pump inlet diameter, D_j=76 mm; hub diameter, d_h=0 mm; impeller output diameter, D_2=137 mm; impeller output width, b_2=14 mm; impeller blade angle, β_2=30°; blade number, Z=6; scroll of blade, 104.5°; volute basic circle diameter, D_3=145 mm; volute entry width, b_3=30 mm.

2.2 Computational grid

To effectively compute convergence and eliminate the negative effects of the velocity of uniform incoming flow, we extended the straight tube suction chamber and pump outlet appropriately. The computing domain was mesh-generated by using the GAMBIT2.3.16 software, and the results are shown in Figure 1. A tetrahedral mesh was adopted in the impeller and volute. The grid numbers were 435,530 and 597,127. A hexahedral mesh was adopted in the suction chamber and outlet extension section. The grid numbers were 152,827 and 54,944. The total grid number of the entire computing domain was 1,240,428. Through a quality check of the grid, we found that the isometric slope and equal-sized slope were all lower than 0.83. The slopes near the walls Y+ were approximately 30, and the grid was of high quality.

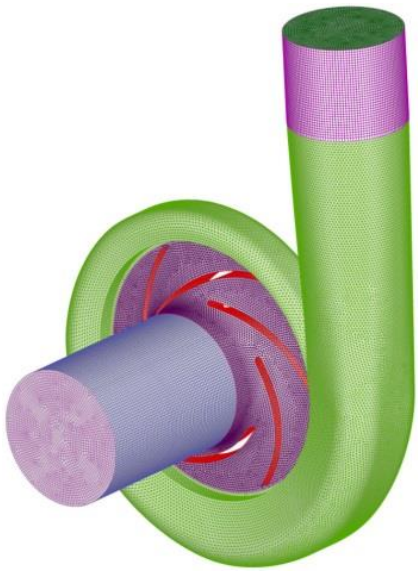

Figure 1: Computing domain and grid

2.3 Multiphase model

Based on the Euler method of the mixture algebraic slip model, the multiphase model of the numerical calculation was used to simulate a silt–liquid two-phase turbulent flow. In the computing process, the particle was treated as pseudo-fluid.

The equation of continuity of the mixture model is

$$\frac{\partial}{\partial t}(\rho_m)+\frac{\partial}{\partial x_i}(\rho_m \boldsymbol{u}_{m,i})=0\,. \tag{1}$$

ρ_m is the mixture density, and $\boldsymbol{u}_m$ is the average mass velocity. Momentum equation is

$$\frac{\partial}{\partial t}(\rho_m u_{m,j})\frac{\partial}{\partial x_i}(\rho_m u_{m,i}u_{m,j})=-\frac{\partial p}{\partial x_j}+\frac{\partial}{\partial x_i}\times\mu_m\left(\frac{\partial u_{m,i}}{\partial x_j}+\frac{\partial u_{m,j}}{\partial x_i}\right)+\rho_m g_j+\boldsymbol{F}_j+\frac{\partial}{\partial x_i}\left(\sum_{k=1}^{n}\varphi_k\rho_k u_{D,k,i}u_{D,k,j}\right) \tag{2}$$

P is pressure, μ_m is the mixture virtual viscosity, g is the gravity acceleration, $\boldsymbol{F}$ is the body force, φ is the volume fraction, and $u_{D,k}$ is the drift velocity.

Volume fraction equation is

$$\frac{\partial}{\partial t}(\varphi_s\rho_s)+\frac{\partial}{\partial x_i}(\varphi_s\rho_s u_{m,i})=-\frac{\partial}{\partial x_i}(\varphi_s\rho_s u_{D,s,i}) \tag{3}$$

$$\rho_m=\sum_{k=1}^{n}\varphi_k\rho_k \qquad \mu_m=\sum_{k=1}^{n}\varphi_k\mu_k \qquad \boldsymbol{u}_m=(\sum_{k=1}^{n}\varphi_k\rho_k\boldsymbol{u}_k)/\rho_m \tag{4}$$

Drift velocity of the K[th] term is

$$\boldsymbol{u}_{D,k}=\boldsymbol{u}_k-\boldsymbol{u}_m=\boldsymbol{v}_{k,c}-\frac{1}{\rho_m}\sum_{i=1}^{n-1}\varphi_i\rho_i\boldsymbol{v}_{i,c} \tag{5}$$

Drift velocity of the K[th] term is

$$\boldsymbol{v}_{k,c}=\frac{(\rho_m-\rho_k)d_k^2}{18\mu_c\mu}\left[\left(\boldsymbol{g}-\frac{D\boldsymbol{u}_m}{Dt}\right)\right] \tag{6}$$

$$\mu=\begin{cases}1+0.05Re^{0.687} & Re<1\ 000\\ 0.018Re & Re\geq 1\ 000\end{cases} \tag{7}$$

M is the friction coefficient, d is the particle diameter, μ_c is the continuous item viscosity, and Re is the Reynolds number. The steady flow in a jet pump was calculated with the above equation without phase shifting varying rates.

2.4 Solution setup

The RNG k–ε two-equation model was adopted in this research to make the average Reynolds equation a closure model. During the computing process, the stimulation of the rotor/stator interaction was achieved through the frozen rotor method. The inlet velocity and free discharge were selected as the boundary conditions in the inlet and outlet. To achieve an accurate numerical simulation, we calculated the turbulent energy and turbulent dissipation rate with the inlet boundary condition specified. In the near wall area with a low Reynolds number, standard wall functions were adopted to solve the problems brought about by the turbulence model with a high Reynolds number. The coupling calculation of velocity and pressure was achieved by the SIMPLE algorithm. The first-order upwind difference scheme, second-order central difference schemes, and the linearized standard format were adopted for the spatial dispersions of the advection term, diffusive term, and source term, respectively. The solid particles were assumed to be uniform and spherical. The convergence criterion for each governing equation was 0.0001.

2.5 Computational scheme

computational condition	Q=50m^3/h，d=0.10mm，ρ=2500kg/m^3				
solid concentration	1%	5%	10%	15%	20%

III. RESULTS ANALYSIS

3.1 External characteristics

The pump inlet and outlet pressure and the external characteristics are shown in Figures 2 and 3, respectively. As shown in Figure 2, when the solid-phase concentrations of the transported solid–liquid two-phase flow were 1%, 5%, 10%, 15%, and 20%, the pump inlet pressures were −0.460, −0.414, −0.358, −0.288, and −0.222 kPa, respectively; and the pump outlet pressures were 193.856, 169.546, 153.524, 146.127, and 142.893 kPa, respectively. As the solid-phase concentration increased, the pump inlet pressure gradually rose while the outlet pressure decreased. Although the pump inlet pressure rose with the increase in the concentration, the

increase in the absolute change value was small. As for the pump outlet pressure, it showed a drastic decline.

The computing results of the external characteristics are shown in Figure 3. When the solid-phase concentrations in the transported solid–liquid two-phase flow were 1%, 5%, 10%, 15%, and 20%, the computational lift values were 19.70, 16.29, 13.81, 12.36, and 11.39 m, respectively; the computational efficiency values were 72.13%, 57.82%, 47.49%, 41.65%, and 37.79%, respectively; and the computational shaft power values were 3.773, 4.122, 4.551, 4.948, and 5.333 kW. As the transported solid-phase concentration rose, the computational lift and efficiency increased accordingly while the computational shaft power monotonically increased.

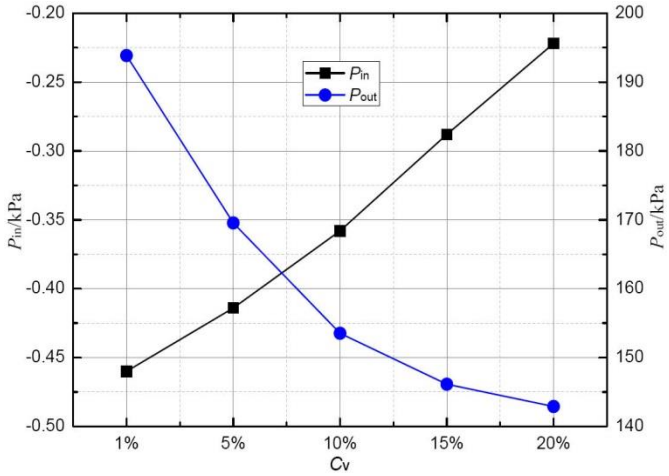

Figure 2: Influence of solid-phase concentration on pump inlet and outlet pressure

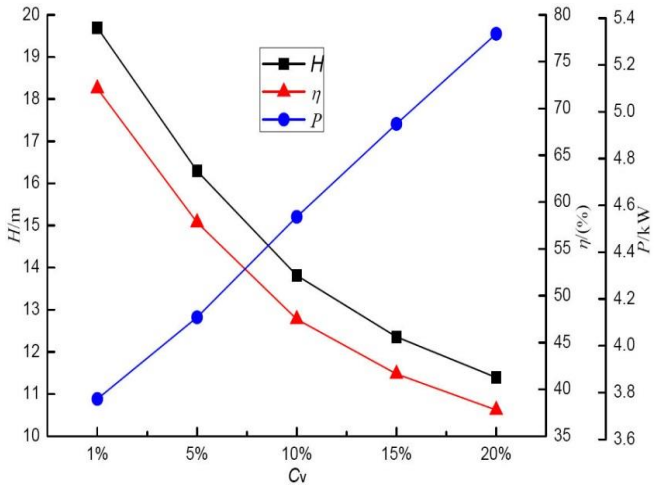

Figure 3: Influence of solid-liquid two-phase concentration on the external characteristics of the pump

3.2 Pressure surface characteristic

The influence of the solid-phase concentration on the performance parameter of the pressure surface of the blade is depicted in Figure 4. Figure 4(a) shows the influence of total vane pressure distribution. The total pressure on the vane rose with the increase in the blade radius. Therefore, we can infer that the second part of the vane pressure surface mainly caused the increase in pressure. As the computational concentration increased, the total vane pressure showed a tendency to gradually decrease. Under 1% computational concentration and when the relative length was larger than 0.7, the total pressure increased slowly. The corresponding transport concentrations were 1%, 5%, 10%, 15%, and 20%. At the front part of the vane pressure surface, the total pressures were 33.086, 18.687, 6.419, −0.815, and −5.245 kPa. When the relative length was 0.5, which indicated a mid-position, the total pressures were 191.794, 173.952, 167.6, 167.776, and 172.149 kPa. At the trailing edge of the vane, the total pressures were 212.118, 212.973, 221.334, 231.134, and 241.501 kPa. At the same position, the high pressure caused the total pressure to decline because of the jet-wake flow.

The distribution of the solid-phase concentration on the vane is illustrated in Figure 4(b). As the transported solid-phase concentration increased, the solid-phase concentration continuously rose at any radius location. This result is attributed to the increased number of particles. Under the condition of any transported concentration, the solid-phase concentration increased minimally after a sharp decrease. When the transported concentrations were 1%, 5%, 10%, 15%, and 20%, the volume concentrations of the solid particles were 0.947%, 5.33%, 10.187%, 14.307%, and 18.872%, respectively. At the mid-position of the vane pressure surface, the solid-phase concentrations were 0.105%, 1.35%, 3.343%, 5.277%, and 7.686%. At the trailing edge of the vane, the solid-phase concentrations were 0.633%, 3.332%, 6.908%, 10.294%, and 13.705%.

As for the vortex in Figure 4(c), its distribution characteristics were similar under the four different concentrations of 5%, 10%, 15%, and 20% and showed minimal variation. However, when the transported concentration was 1%, the distribution characteristics along the pressure surface were different from those in the above situations. As for the concentrations of 5%, 10%, 15%, and 20%, the vortex values at the front part of the pressure surface were 3257.89, 13750.8, 14569.1, 14935.8, and 15016.4 s^{-1}. At the trailing edge of the vane pressure surface, the vortex values were 3416.81, 7428.78, 8697.33, 8217.54, and 7922.65 s^{-1}. The kinetic energy (Figure 4(d)), the turbulent energy dissipation rate (Figure 4(e)), and the turbulence intensity (Figure 4(f)) showed the same changes, that is, they all increased with the rise in the transported solid-phase concentration. However, for any transported solid-phase concentration, the kinetic energy, turbulent energy dissipation rate, and turbulence intensity gradually decreased to the minimum value from the front part and then increased. The three parameters effectively indicate the flow characteristics of the solid–liquid two-phase flow in the pump.

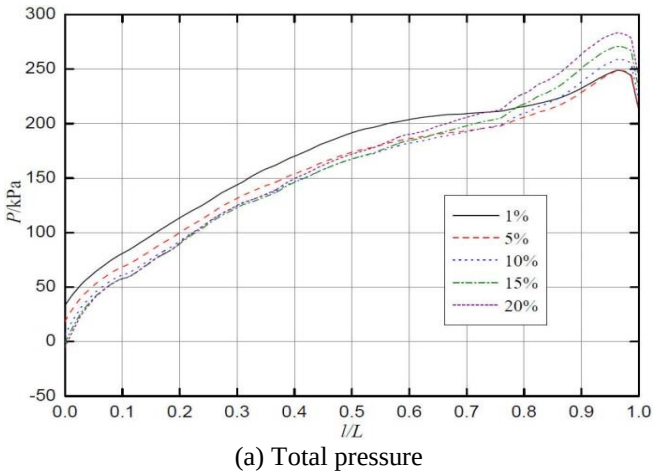

(a) Total pressure

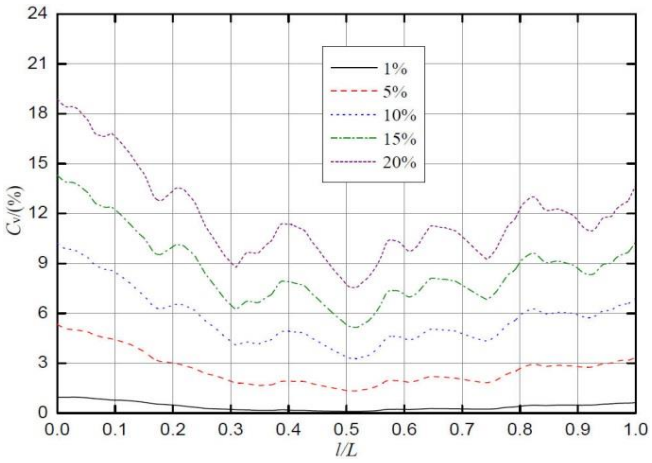

(b) Solid-phase concentration

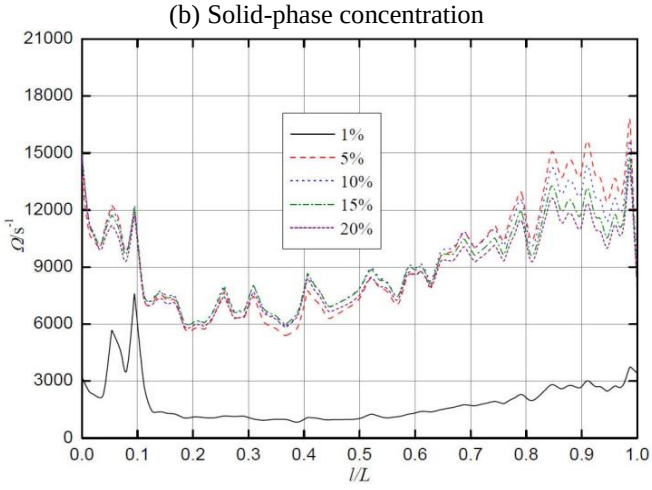

(c) Vortex

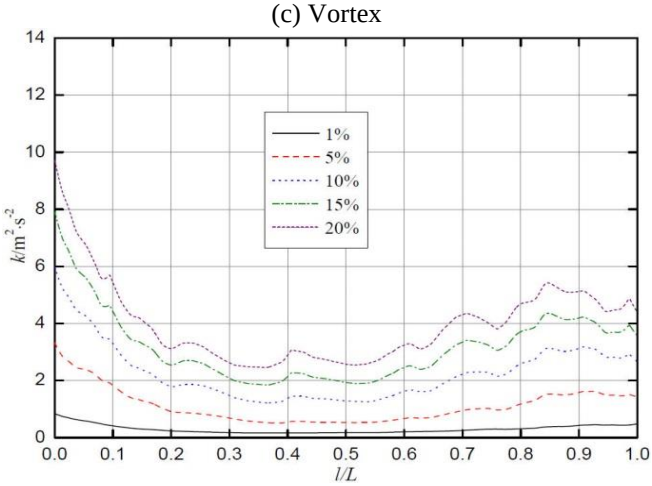

(d) Kinetic energy

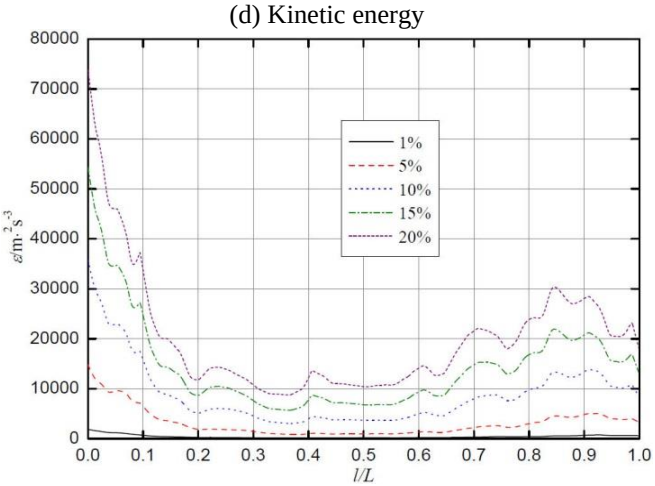

(e) Turbulent dissipation rate

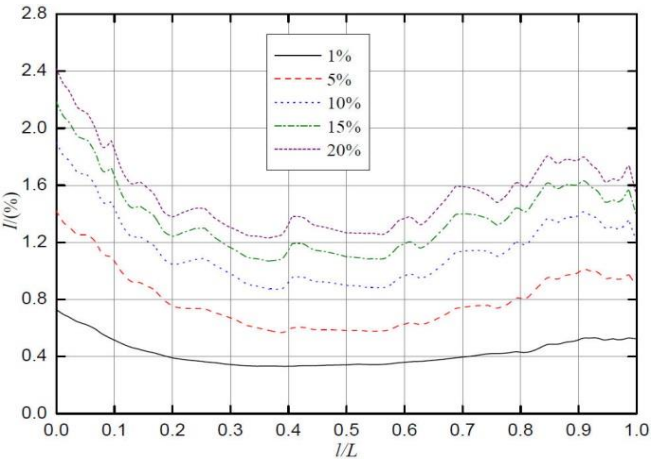

(f) Turbulence intensity

Figure 4: Influence of solid-phase concentration on the performance parameters of the vane pressure surface

3.3 Suction surface characteristics

The influence of the solid-phase concentration on the performance parameter of the vane pressure surface is shown in Figure 5. Figure 5(a) shows the influence of total vane pressure distribution. The total pressure always showed the tendency to rise with the increase in the radius from the front part of the suction surface under any transported concentration. A dramatic drop was observed at the outlet of the suction surface, similar to the previous discussion. Generally, the total pressure on the suction surface increased as the transported solid-phase concentration rose. The difference was the increasing range. When the relative length was smaller than 0.5, the increasing difference in pressure was not obvious. However, at the secondary part of the suction surface, the increasing difference in pressure was obvious. As for the concentrations of 5%, 10%, 15%, and 20%, the total pressures at the front part of the suction surface were −44.844, −40.356, −35.976, −32.815, and −30.666 kPa. At the mid-position of the suction surface, the total pressures were 62.362, 62.598, 73.698, 86.119, and 101.852 kPa. At the position in which the relative length was 0.9, the total pressures were 199.551, 281.383, 339.416, 365.957, and 401.358 kPa.

The influence of the transported solid-phase concentration on the distribution of the solid-phase concentration on the vane suction surface is shown in Figure 5(b). With the increase in the transported solid-phase concentration, the solid-phase concentration on the vane suction surface continuously increased. This result is directly attributed to the increasing solid particles in the pump. When the transported solid-phase concentration was 1%, the solid-phase concentration on the vane suction surface was low and showed minimal change. The corresponding solid-phase concentrations to the front part of the vane, the mid-position of the vane, and the trailing edge of the vane were 0.9%, 0.818%, and 1.545%, respectively. However, when the concentrations were 5%, 10%, 15%, and 20%, no obvious increase was observed at the front part of the vane, but an obvious increase was noted at the trailing edge position. At the front part of the suction surface, the four corresponding solid-phase concentrations were 4.356%, 9.374%, 14.798%, and 20.173%. At the mid-position of the suction surface, the four corresponding solid-phase concentrations were 4.902%, 12.236%, 19.808%,

and 29.379%. At the position in which the relative length was 0.9, the four corresponding solid-phase concentrations were 10.145%, 21.022%, 27.686%, and 35.059%. Thus, we can infer that, under high transported solid-phase concentrations, wear occurred mainly in the secondary part of the suction surface.

The vortex distributions on the vane suction surface under different transported solid-phase concentrations are shown in Figure 5(c). Except for the case in which the transported solid-phase concentration was 1%, the other cases showed similar vortex distributions on the vane suction surface. As for the case in which the transported solid-phase concentration was 1%, when the relative length was shorter than 0.68, the vortex showed a small ripple with a stable average value, but the vortex was high at the inlet position of the suction surface. At the secondary part of the suction surface, the vortex rose markedly. When the relative lengths were 0.4, 0.6, and 0.8, the vortexes were 4030.34, 3548.85, and 13084.3 s^{-1}, respectively. The distribution of the kinetic energy, the turbulent energy dissipation rate, and the turbulence intensity along the vane suction surface under different transported solid-phase concentrations are shown in Figures 5(d), 5(e), and 5(f), respectively. The three parameters showed a similar change, that is, they all increased with the increase in the transported solid-phase concentration.

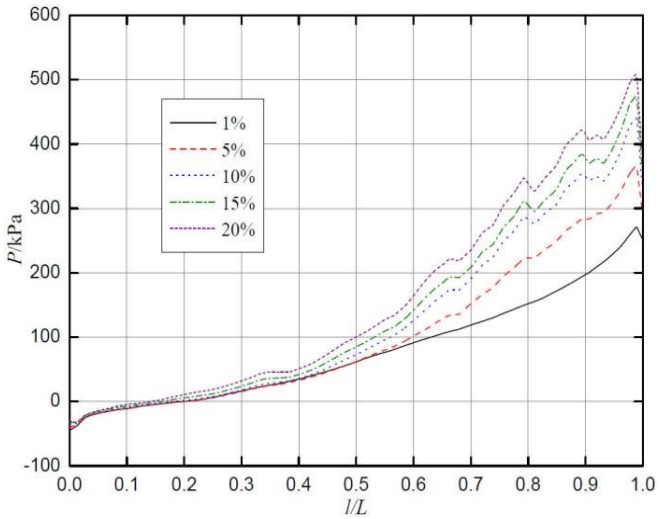

(a) Total pressure

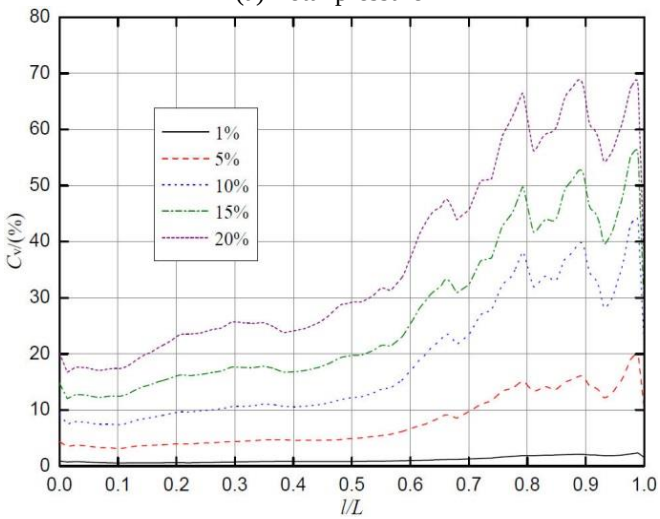

(b) Solid-phase concentration

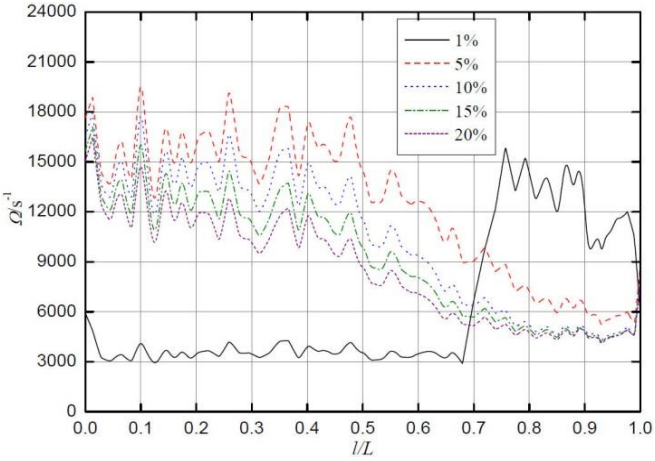

(c) Vortex

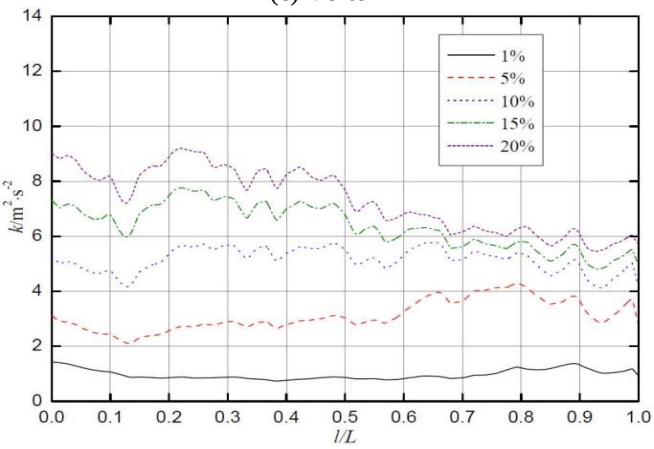

(d) Kinetic energy

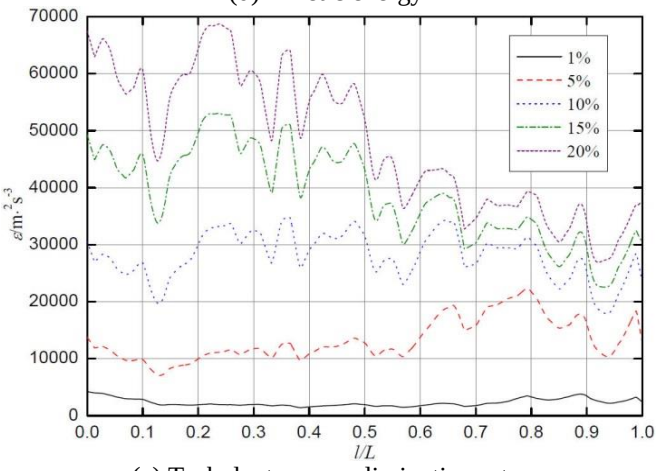

(e) Turbulent energy dissipation rate

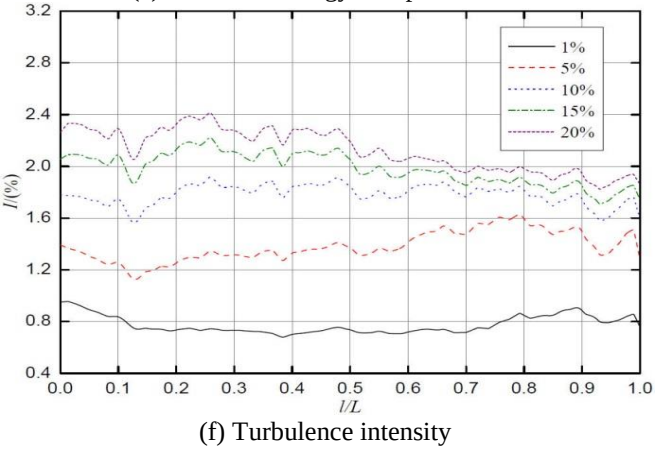

(f) Turbulence intensity

Figure 5: Influence of solid-phase concentration on the performance parameters of the vane pressure surface

3.4 Total pressure distribution on the vane under different solid-phase concentrations

The total pressure distribution on the pressure and suction surface of the vane under five different transported solid-phase concentrations is shown in Figure 6. Apparently, the total pressure rose with the increase in the radius regardless of the pressure surface or suction surface. When the transported solid-phase concentration was 1%, which was regarded as low, the total pressure on the pressure surface in most areas (in which the relative length was 0.96) was always higher than that on the suction surface; the opposite occurred thereafter. In summary, the isostatic pressure balance point of the pressure surface and suction surface was at the area in which the relative length was 0.96. As for the other four transported solid-phase concentrations, similar changes were observed; the only difference was the location of the isostatic pressure balance point. When the transported solid-phase concentrations were 5%, 10%, 15%, and 20%, the positions of the isostatic pressure balance point were 0.77, 0.70, 0.67, and 0.63, respectively. With the increase in the transported solid-phase concentration, the isostatic pressure balance point continuously moved toward the leading edge.

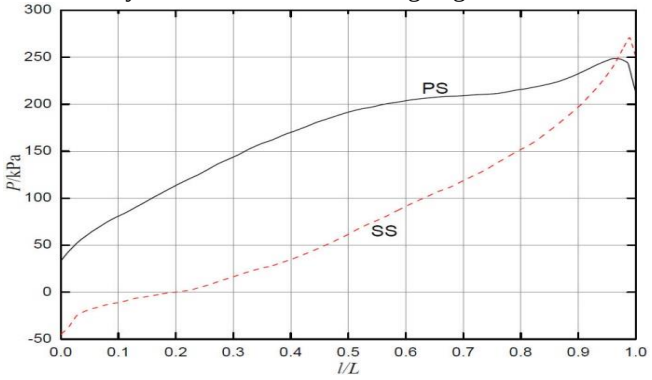

(a)1%

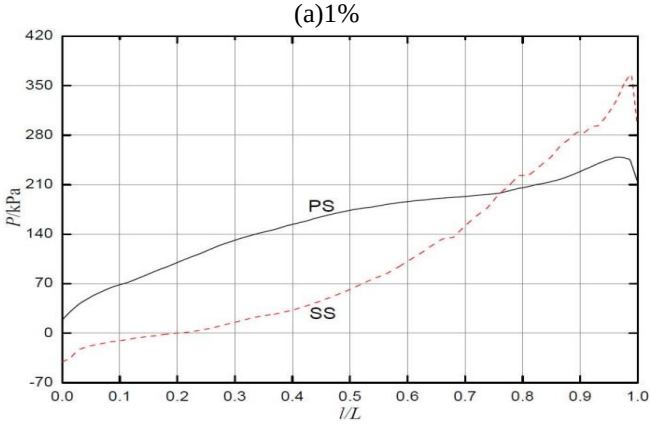

(b)5%

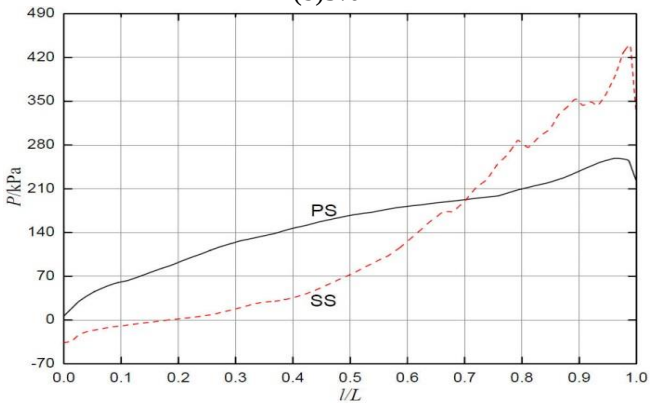

(c)10%

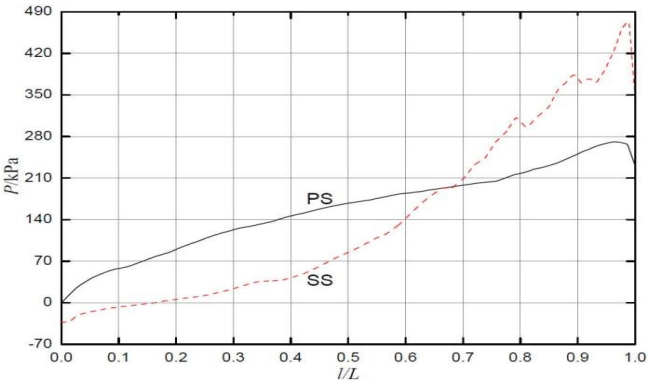

(d)15%

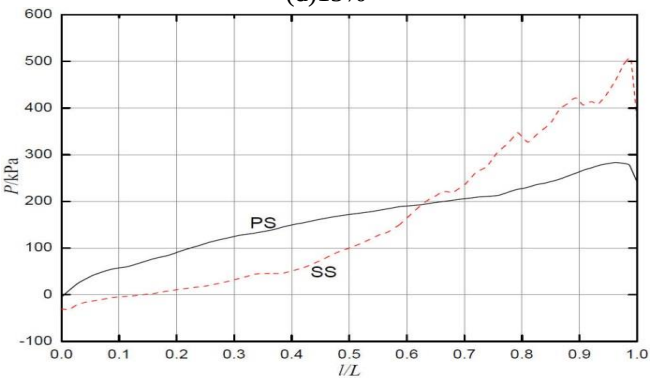

(e)20%

Figure 6: Change of total pressure distribution on the vane under different solid-phase concentrations

3.5 Distribution of particle concentration on the vane under different solid-phase concentrations

The distribution of the solid-phase concentration on the pressure and suction surface of the vane under five different transported solid-phase concentrations is shown in Figure 7. In most areas of the vane surface, the solid-phase concentration of the suction surface was higher than that of the pressure surface. Given that the solid-phase concentration reflected the wear degree of the wall surface to some extent, we can infer that the suction surface could bear serious wear. Moreover, the position of the isoconcentration point (the point of the same solid-phase concentration at the same radius of the pressure surface and suction surface) constantly changed. When the concentrations were 1%, 5%, 10%, 15%, and 20%, the positions of the isoconcentration point were 0.16, 0.15, 0.13, 0.10, and 0.07, respectively. That is, as the transported solid-phase concentration increased, the isoconcentration point of the pressure surface and suction surface moved toward the inlet of the vane.

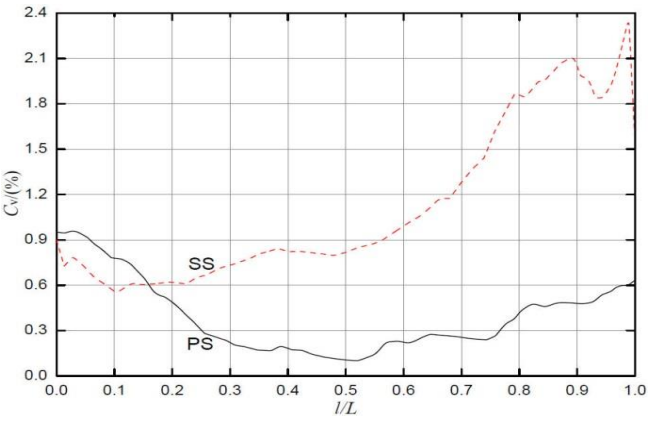

(a)1%

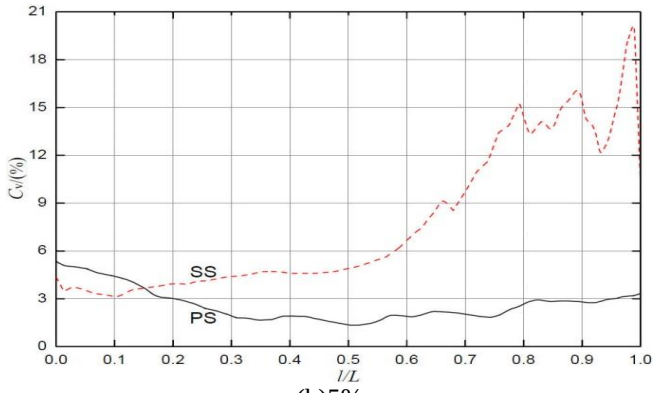

(b)5%

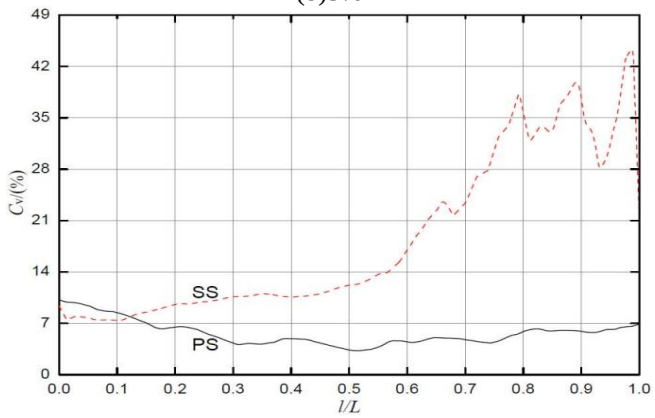

(c)10%

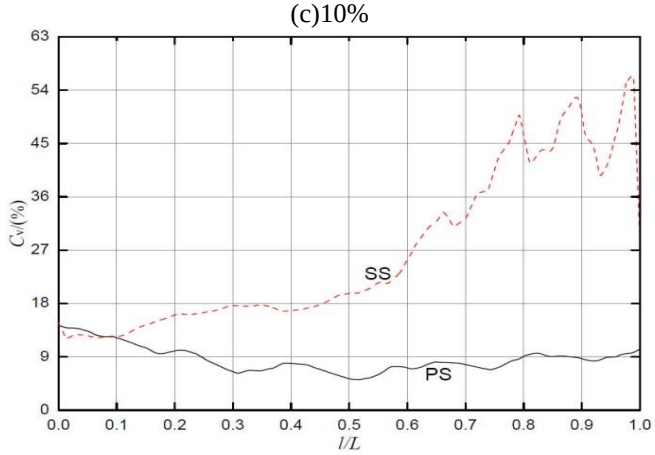

(d)15%

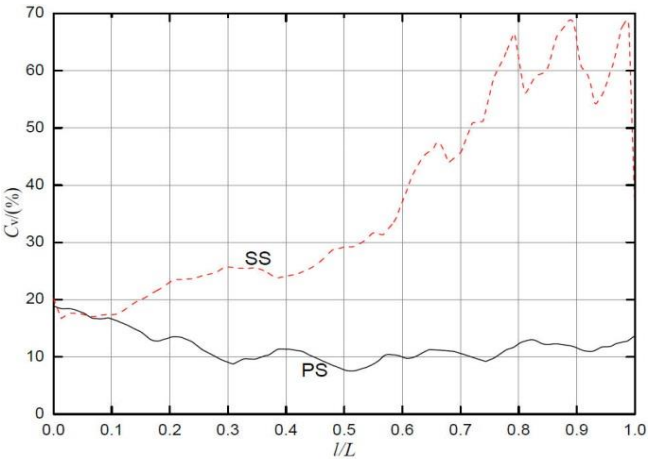

(e)20%

Figure 7: Changes of the distribution of the solid-phase concentration on the vane under different solid-phase concentrations

3.6 Particle concentration of the pressure surface on the vane

The distribution of the particle concentration of the pressure surface on the vane under five different transported solid-phase concentrations is shown in Figure 8. When the transported concentration was low at 1%, the distribution of the particle concentration of the pressure surface on the vane was an even one. When the concentration was 5%, the solid-phase concentration at the inlet and outlet of the pressure began to rise. When the concentrations were 10%, 15%, and 20%, the solid-phase concentration at the inlet and outlet of the pressure surface was high. These results indicate that the above position would suffer from severe wear.

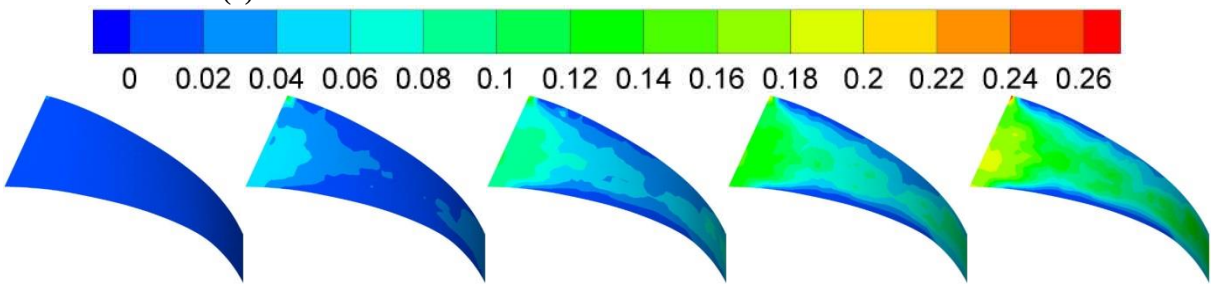

(a)1% (b)5% (c)10% (d)15% (e)20%

Figure 8: Distribution change of the particle concentration of the pressure surface on the vane under different solid-phase concentrations

3.7 Particle concentration of the pressure surface on the vane

The distribution of the particle concentration of the suction surface on the vane under five different transported solid-phase concentrations is shown in Figure 8. When the transported concentration was low at 1%, the distribution of the particle concentration of the suction surface on the vane was an even one. When the concentration was 5%, the solid-phase concentration at the secondary part of the pressure began to rise. When the concentrations were 10%, 15%, and 20%, the solid-phase concentration at the inlet and outlet of the suction surface was high. These results indicate that the above position would suffer from severe wear.

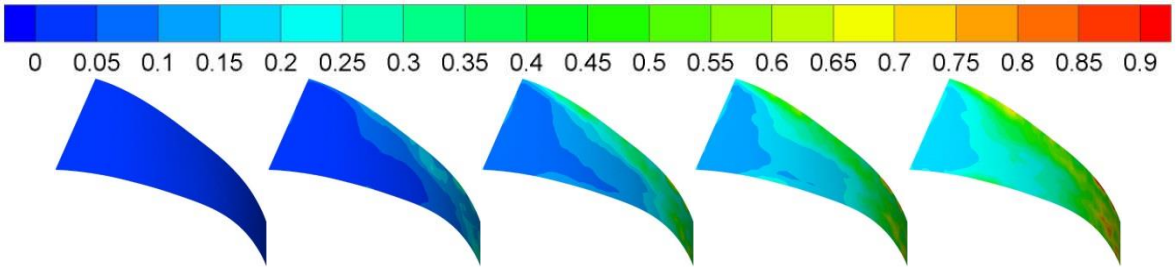

(a)1% (b)5% (c)10% (d)15% (e)20%

Figure 9: Distribution change of the particle concentration of the suction surface on the vane under different solid-phase concentrations

3.8 Particle concentration of the volute surface

The distribution of the particle concentration of the volute surface under five different transported solid-phase concentrations is shown in Figure 10. Regardless of amount of transported concentration (1% or 20%), the distribution of the particle concentration of the volute surface was even, which indicated that the degree of inner surface wear of the volute was approximately in agreement with each other. When the concentration was 5%, the distribution of the particle concentration of the volute inner surface was uneven; at the position near the volute tongue, the highest concentration could reach 30%. Such a situation also occurred when the transported solid-phase concentrations were 10% and 15%. The position near the volute tongue still had a high solid-phase concentration, which indicated that, under the corresponding situations, the aforementioned positions would suffer from severe wear.

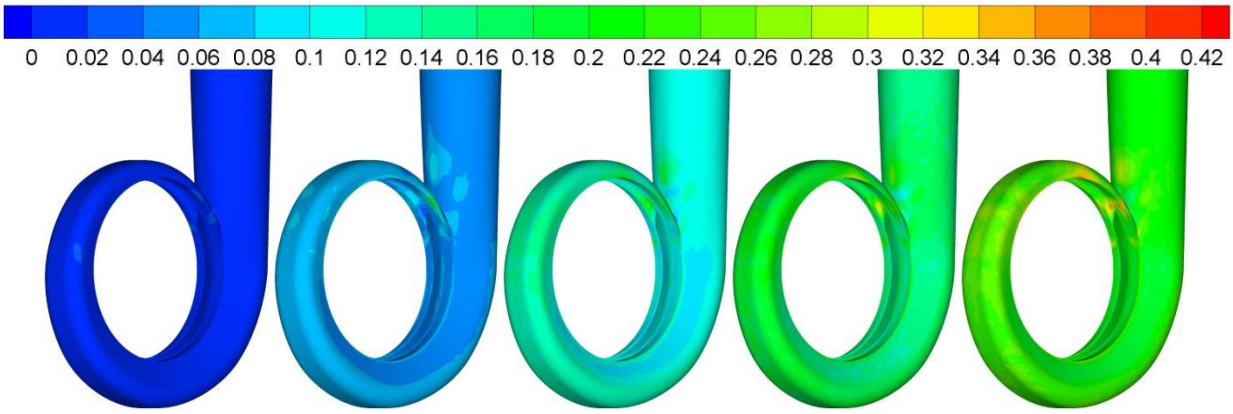

(a)1% (b)5% (c)10% (d)15% (e)20%

Figure 10: Distribution change of the particle concentration of the volute surface on the vane under different transported solid-phase concentrations

3.9 Total pressure and streamline

The placement of the total pressure and streamline under different transported solid-phase concentrations is shown in Figure 11. When the transported solid-phase concentrations differed, the streamline distinction in each channel of the vane wheel was not obvious and was approximately in agreement with those in other channels. This outcome can be explained by the fact that, although the transported solid-phase concentrations differed, the computation conditions were all design conditions that favored the corresponding inner flow.

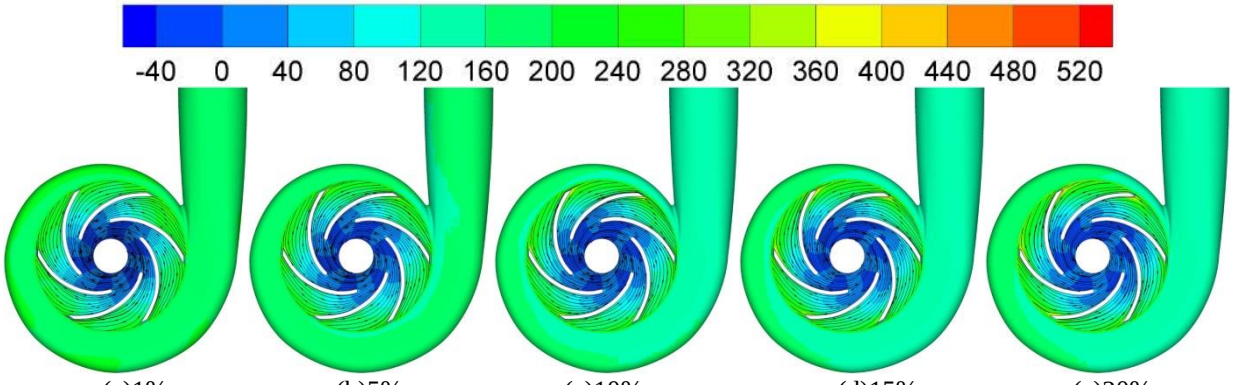

(a)1% (b)5% (c)10% (d)15% (e)20%

Figure 11: Placement of the total pressure and streamline under different transported solid-phase concentrations

IV. CONCLUSIONS

With the increase in the transported solid-phase concentration, the total pressure of the pump inlet showed a tendency to gradually rise. By contrast, the total pressure of the pump outlet showed a tendency to gradually decline. Although the total pressure of the pump inlet increased with the increasing transported solid-phase concentration, its absolute variation value was small. By contrast, the decrease in the total pressure of the pump outlet was severe.

With the increase in the transported solid-phase concentration, the computational lift and efficiency of the pump decreased monotonously. Under the same condition, the shaft power monotonically increased.

With the increase in the transported solid-phase concentration, the solid-phase concentration on the vane suction surface continuously rose. Regardless of the amount of transported concentration, the solid-phase concentration showed a tendency to increase minimally after a sharp decrease. When the transported solid-phase concentration was high, the secondary part of the suction surface mainly suffered from wear.

With the increase in the transported solid-phase concentration, the isostatic pressure balance point continuously moved toward the leading edge, and the isoconcentration point of the pressure surface and suction surface moved toward the inlet of the vane.

ACKNOWLEDGEMENT

The work was supported by the Zhejiang Provincial Natural Science Foundation of China (No.LY14E090011), Zhejiang Provincial Science and Technology Project (No.2015C31129), Academic Foundation of Quzhou University (No.XNZQN201508), and Chinese National Foundation of Natural Science (No.51536008, 51505253).

REFERENCES

[1]Engin T, Gur M. Performance characteristics of centrifugal pump impeller with running tip clearance pumping solid-liquid mixtures[J]. Journal of Fluids Engineering, 2001, 123(3): 532-538.

[2]Gandhi B K, Singh S N, Seshadn V. Effect of speed on the performance characteristics of a centrifugal slurry pump[J]. Journal of Hydraulic Engineering, 2002, 128(2): 225-233.

[3]Yuan Shouqi, Zhang Peifang, Zhang Jinfeng. Numerical simulation of 3-D dense solid- liquid two- phase turbulent flow in a non-clogging mud pump[J]. Chinese Journal of Mechanical Engineering, 2004, 17(4):623-627.

[4]Li Yi, Zhu Zuchao, He Weiqiang, et al. Numerical simulation and experimental research on the influence of solid phase characteristics on centrifugal pump performance[J]. Chinese Journal of Mechanical Engineering, 2012, 25(6): 1184-1189.

[5]Zhang Yuliang, Li Yi, Cui Baoling, et al. Numerical simulation and analysis of solid-liquid two-phase flow in centrifugal pump[J]. Chinese Journal of Mechanical Engineering, 2013, 26(1): 53-60.

[6]Zhang Yuliang, Li Yi, Zhu Zuchao, et al. Computational analysis of centrifugal pump delivering solid-liquid two-phase flow during startup period[J]. Chinese Journal of Mechanical Engineering, 2014, 27(1): 178-185.

[7]Harry H T, Graeme R A. Experimental study on erosive wear of some metallic materials using Coriolis wear testing approach[J]. Wear, 2005, (258): 458-469.

[8]Veselin B. Erosive wear model of slurry pump impeller[J]. Journal of Tribology, 2010, 132(2): 021602.1-5.

LI Xin, College of Mechanical Engineering, Quzhou University, Quzhou 324000, China, Key Laboratory of Advanced Manufacturing Technology of Zhejiang Province, Hangzhou 310027, China

ZHANG Yu-liang, College of Mechanical Engineering, Quzhou University, Quzhou 324000, China,

YU Jian-ping, College of Mechanical Engineering, Quzhou University, Quzhou 324000, China,

ZHOU Zhao-zhong, College of Mechanical Engineering, Quzhou University, Quzhou 324000, China,